Description and climatology of a new general circulation model of the Martian atmosphere

Paul Hartogh, Alexander S. Medvedev, Takeshi Kuroda, Ryu Saito, and Geronimo Villanueva
Max Planck Institute for Solar System Research, Katlenburg-Lindau, Germany

Artem G. Feofilov and Alexander A. Kutepov
Institute for Astronomy and Astrophysics, University of Munich, Munich, Germany

Uwe Berger
Leibniz Institute of Atmospheric Physics, Kühlungsborn, Germany

Received 20 May 2005; revised 7 September 2005; accepted 14 September 2005; published 30 November 2005.

[1] The paper presents a new grid point global general circulation model (GCM) for the Martian atmosphere with the vertical domain extending from the surface into the lower thermosphere (around 130 km). The model contains the comprehensive physical parameterizations relevant to this altitude range, including a novel CO_2 15 μm band radiation scheme for the non-LTE. The performance of the model is shown in the zonal mean fields simulated for several seasons. The comparison demonstrates a good agreement with the temperature measurements by the Thermal Emission Spectrometer below 40 km and an overall agreement with the results from other Martian GCMs. The model was used to demonstrate that the global meridional transport during solstices is forced primarily by eddies and that the ability of the model to simulate the winter polar warming depends on the ability to resolve the longitudinal disturbances, both topographically and radiatively generated.

Citation: Hartogh, P., A. S. Medvedev, T. Kuroda, R. Saito, G. Villanueva, A. G. Feofilov, A. A. Kutepov, and U. Berger (2005), Description and climatology of a new general circulation model of the Martian atmosphere, *J. Geophys. Res.*, *110*, E11008, doi:10.1029/2005JE002498.

1. Introduction

[2] General circulation models (GCMs) of the Martian atmosphere are becoming increasingly sophisticated both due to improved parameterizations of physical processes, and due to more data from space missions and ground-based observations. Beginning with the early Martian GCM of *Leovy and Mintz* [1969], many terrestrial models have been adapted to simulate the global Martian weather and climate, [e.g., *Haberle et al.*, 1993; *Hourdin et al.*, 1995; *Wilson and Hamilton*, 1996; *Forget et al.*, 1999; *Takahashi et al.*, 2003; *Moudden and McConnell*, 2005; *Kuroda et al.*, 2005]. These GCMs rely on the numerous data obtained with the very successful missions to Mars of Viking, Mars Pathfinder, Mars Global Surveyor, Mars Express. Current and future planned space (e.g., Mars Climate Sounder on board the Mars Reconnaissance Orbiter), airborne (e.g., Stratospheric Observatory For Infrared Astronomy/German REceiver for Astronomy at Terahertz Frequencies - SOFIA/GREAT), and ground-based (e.g., the SubMillimeter Array - SMA, and the Atacama Large Millimeter Array - ALMA) instruments will provide vertical samplings of temperature, wind, and constituents on Mars from the surface into the middle and upper atmosphere. As with the Earth atmosphere, GCMs are and will be an invaluable tool in analyzing and interpreting these data.

[3] We present here a new general circulation model which was developed under the aegis of the Mars Atmosphere Observation and Modeling project (MAOAM) as part of the German Research Foundation (Deutsche Forschungsgemeinschaft, DFG) research priority program "Mars and the Terrestrial Planets". The origination of this model can be traced back to the Cologne Model of the Middle Atmosphere (COMMA) [*Rose*, 1983; *Berger and von Zahn*, 1999], and its first Martian counterpart [*Ebel and Berger*, 1997]. The model was completely re-designed to accommodate for more effective numerical procedures and parallel processing [*Villanueva*, 2004]. Significant changes were introduced to its dynamical core, in particular to the discretization, time integration scheme, horizontal diffusion and near pole filtering. In the model we are to report on, some physical parameterizations have been adapted from terrestrial GCMs (e.g., vertical turbulent diffusion, surface physics, gravity wave drag), some have been adapted from other Martian GCMs (e.g., CO_2 near-infrared heating, dust radiation), and the new ones have been added (15 μm CO_2 cooling scheme, and the gravity wave drag parameterization

0148-0227/05/2005JE002498

coupled to orographic sources). The top of the model is taken at around 130 km, high enough to resolve the meridional transport cell and therefore to describe reasonably well the circulation below [e.g., *Forget et al.*, 1999]. The heights between approximately 110 and 130 km divide two atmospheric regions with differing dynamical regimes. The thermosphere above is primarily driven by the solar forcing, and the molecular viscosity there is strong enough that it dominates the dynamics. Below in the mesosphere, the effect of viscosity is weak, and the atmosphere is much more subjected to an internal variability. Meaningful results presented in this paper are below 110 km because (1) we do not include parameterizations suitable for the thermosphere and (2) this area is less affected by the lid of the model domain through the downward control [*Shepherd et al.*, 1996] and wave reflection. The specifics of the mesosphere are the breakup of the local thermodynamic equilibrium (LTE) [*Andrews et al.*, 1987] above approximately 80–90 km with the maximum of the non-LTE cooling effects at around 130–140 km, and a possible impact of breaking gravity waves. There are very few observational data above 60 km to constrain both the model and gravity wave schemes. The rationale of this paper is to present a zonal mean climatology produced by the model, and to compare it with the available to us global measurements and with the results from other Martian GCMs. The model was applied to demonstrate that the global meridional transport during solstices is forced primarily by eddies, and that the strength of the winter polar warming strongly depends on them.

[4] Section 2 presents a general description of the model and its dynamical core. Physical parameterizations are described in sections 3–6. Results of the simulations are shown in section 7. Discussion of the numerical tests to ensure the internal validity of the model, and to study its sensitivity to the variations of some parameters is given in section 8.

2. General Description and Model Dynamics

[5] The model is based on COMMA–IAP (Institute of Atmospheric Physics), a terrestrial GCM which was extensively used for studies of the dynamics and photochemistry in the Middle atmosphere for more than 20 years [e.g., *Jakobs et al.*, 1986; *Berger and Dameris*, 1993; *Berger and von Zahn*, 1999; *Sonnemann and Grygalashvyly*, 2003]. The atmosphere of Mars is significantly less dense than on Earth, wind speeds are larger, and the variations of the field variables are stronger. This and the highly irregular Martian topography contribute to the model instability. To handle simulations under the Martian conditions without resorting to excessively high numerical and imposed diffusivities, we have introduced a number of changes to the original dynamical core of the COMMA–IAP. They are: the time stepping scheme, vertical spacing, horizontal diffusion, and the near pole filtering. These changes to the dynamics have been extensively tested against the benchmark COMMA–IAP model, and represent a careful compromise between the stability, accuracy, conservation properties, and the numerical efficiency.

[6] The dynamical core of the model is the finite-difference (grid point) solver for the hydrostatic primitive equations of the hydrodynamics on the sphere. The equations for the horizontal momentum, the thermodynamic equation as well as the continuity and the hydrostatic equations [e.g., *Andrews et al.*, 1987] are discretized on a regular grid in the flux form. The vertical discretization is based on the log-pressure coordinates $z = -H \log(\rho_0/\rho_s)$, where ρ_0 is the background density profile, ρ_s is the reference density at some height; $H = RT_s/g$ is the scale height, T_s being the constant reference temperature, R is the gas constant; g is the acceleration of gravity. The formulation in terms of the log-pressure coordinates implies that the geopotential Φ is used instead of the pressure. In particular, the prognostic equation for the surface geopotential Φ_s is solved to provide a lower boundary condition.

[7] The model has a variable resolution in both horizontal and vertical, as most of the modern atmospheric GCMs do. The higher resolution can be used for studying the mesometeorology of a particular region of the planet. It is run most often in the "lower resolution" mode (32×36 grid points in the longitude and latitude directions, respectively), and in the "higher resolution" version (64×36) for some experiments. The time step at this resolution is Δt = 2 minutes. 118 vertical staggered levels span the atmosphere from the deepest point on the Martian surface (depends on the horizontal resolution of the model) to approximately 130 km with a vertical grid step of about 1.14 km. Although the vertical spacing can be spread arbitrarily to enhance the resolution near the surface, we found the equidistant separation to be sufficiently adequate, especially in the middle atmosphere. The Martian topography at the lower boundary is implemented using the land-atmosphere mask in the fashion similar to the one normally employed in numerical ocean models. In this study, we use the Mars digital elevation model derived from the Mars Orbiter Laser Altimeter (MOLA) profiles [*Delacourt et al.*, 2003]. The topography was spectrally truncated according to the spatial model resolution, no additional smoothing was performed.

[8] The model utilizes the centered ("leapfrog") time-differencing scheme with the *Asselin* [1972] time filter to suppress computational instabilities that arise from using the second-order approximation for the temporal derivative. For the present vertical domain, we adopt the value of 0.05 for the filter coefficient below 100 km, followed by the tangential rise to 0.15 at 130 km. This vertically increasing time filtering helps to suppress high-frequency oscillations which would require shorter time steps due to the Courant-Friedrich-Levy stability criterion.

[9] The stability of the model is maintained with the use of a "near-pole" Fourier filter [*Takacs and Balgovind*, 1983] at latitudes higher than 82.5 degrees. This filter is applied to the horizontal wind, temperature, and the surface geopotential, and truncates all zonal harmonics higher than 2. In a series of experiments, the model was spun up for 15 sols, and the snapshot fields were inspected for the damage imposed by the filter compared to the test run with extremely short time step and no filter. The truncation wavenumber and the latitudinal position of the filter have been chosen as a compromise between the distortions of the simulated fields and the stability of the model.

[10] To prevent a buildup of the kinetic and potential energy at the shortest resolved spatial scales and the associated instability, a horizontal dissipation is introduced in the form of the *Shapiro* [1970] filter. This filter describes

a subgrid-scale horizontal diffusion and represents an iterated Laplacian operator Δ^n. Effectively, the Shapiro filters approximates the horizontal diffusion in the form $(-\Delta t/\tau_d)(\delta x)^{2n}\ \Delta^n$, where Δt is the time step, τ_d is the dissipation timescale of the disturbance with the scale length δx. In the model, δx coincides with the grid step in the corresponding horizontal direction, and $n = 2$ is used for both the wind and temperature. To enhance model stability and to reflect the much shorter dissipative timescales with decreasing density, we use τ_d exponentially decaying above 100 km.

3. Radiation Schemes

[11] The infrared radiation is a significant physical process in the Martian atmosphere: the 15 μm CO_2 band is the main cooling factor of the entire atmosphere. For a wide range of the atmospheric altitudes, the absorption of the solar radiation in the near infrared provides a significant portion of the atmospheric heating. The middle and upper atmosphere is strongly influenced by the absorption of the infrared radiation coming from the lower atmosphere. Atmospheric mineral dust plays an important role in the radiation budget, especially during dust storm seasons, by absorbing and scattering the solar radiation and emitting in the infrared.

3.1. CO_2 15-μm Cooling

[12] In the middle and upper atmosphere where the frequency of molecular collisions is low, the local thermodynamic equilibrium is broken and the population of ro-vibrational levels of molecules deviates from the Boltzmann law (non-LTE). Accurate calculations of the non-LTE cooling/heating rates require a self-consistent solution of the ro-vibrational relaxation problem and the radiative transfer equation for a large number of ro-vibrational lines. This so-called line-by-line (LBL) approach [*López-Puertas and López-Valverde*, 1995; *Gusev and Kutepov*, 2003] is very time consuming. On the other hand, schemes based on the "cooling-to-space" radiative transfer approximation, although fast, do not provide the desired accuracy [*López-Valverde and López-Puertas*, 2001].

[13] In this model, we applied a new efficient routine for calculating the non-LTE cooling/heating rates in the CO_2 bands in the Martian atmosphere. It represents an optimized version of the exact non-LTE ALI–ARMS (Accelerated Lambda Iteration for Atmospheric Radiation and Molecular Spectra) code described by *Kutepov et al.* [1998] and *Gusev and Kutepov* [2003]. The optimized routine will be presented in detail elsewhere. Here we give only its brief discussion. This scheme (1) utilizes a differential equation approach to solve the radiative transfer equation, and relies on the exact accelerated lambda iteration (ALI) solution [*Rybicki and Hummer*, 1991, and references therein] of the vibrational non-LTE problem; (2) applies the opacity distribution function (ODF) technique [*Mihalas*, 1978] that treats each ro-vibrational band as a single line of a special shape with the detailed accounting for both the Doppler and pressure broadening effects; (3) allows for variable input of all collisional rates and spectroscopic parameters, volume mixing ratios (VMRs), including that for O(3P) atoms; and (4) calculates cooling/heating with a prescribed accuracy by utilizing the optimized sets of vibrational levels and bands. The acceleration of calculations is mainly achieved by applying the ODF, and the acceleration factor is approximately equal to the mean number of lines in the band branches.

[14] As was suggested by one of the reviewers, here we compare the accuracy of the scheme implemented in the model with the ALI–ARMS line-by-line reference model which included 60 vibrational levels of five CO_2 isotopes and 150 ro-vibrational bands. The scheme is about 10^4 times faster than the line-by-line reference model. This acceleration has been achieved (1) by applying the ODF and (2) by utilizing the reduced number of the CO_2 vibrational levels and bands (only fundamental bands of isotopes 626, 636 and 628, and first hot bands of isotope 626 were included).

[15] Figure 1 demonstrates the accuracy of the scheme for the three typical temperature profiles in the Martian atmosphere (left panel) for the night time conditions (only 15 μm CO_2 band is operational). Two of these profiles correspond to the measurements during the Pathfinder (1) and the Viking-1 (2) entries. The third one is taken from the model calculations of *Bougher and Roble* [1991]. The thick lines in the Figure 1 denote the reference calculations. The O(3P) VMR for these calculations was taken from *Nair et al.* [1994]. The absolute error seen in the figure reaches 85 K day^{-1} for the profile No. 3 with the warm mesosphere. It is mostly caused by the reduced set of levels and bands compared to the complete reference model. This error can be decreased by employing a more detailed set. This is demonstrated in Figure 1 for the profile No. 3 where we included additionally the second hot bands of the main isotope 626 and the first hot bands of the isotopes 636 and 628. The corresponding error in cooling rates is reduced by a factor 2, however, at the expense of the computing time (which increased by a factor of about 2 as well). The set of the input parameters for the scheme used in our GCM simulations was taken as a compromise between the accuracy and the computing cost.

[16] We use the same scheme for estimating the cooling/heating rates at all altitudes down to the surface. The ODF approach in the LTE region works, in general, similar to the narrow band technique. This allows for a direct accounting of the radiative properties of the ground, because the differential radiative transfer equation solved by the scheme uses the radiation from the surface as a lower boundary condition. Compared to the line-by-line calculations, the ODFs overestimate cooling near the ground. We minimized this error to 1–2 K day^{-1} by modifying the shape of ODFs in the lower atmosphere.

3.2. CO_2 Near-Infrared Absorption

[17] The routine described above allows us to calculate the heating effect due to the absorption of the solar near-infrared radiation. This, however, decelerates the total CO_2 radiation calculations by a factor of about 3 due to the increased number of the bands which have to be accounted for. Fortunately, this solar add-on to non-LTE cooling/heating rates depends mainly on the pressure and solar zenith angle [*Forget et al.*, 1999], and in the lesser extent, on temperature. In the central panel of Figure 2, we plotted the exact solar add-ons due to the absorption in the near-infrared bands for the overhead solar conditions computed with our reference line-by-line model for the three typical

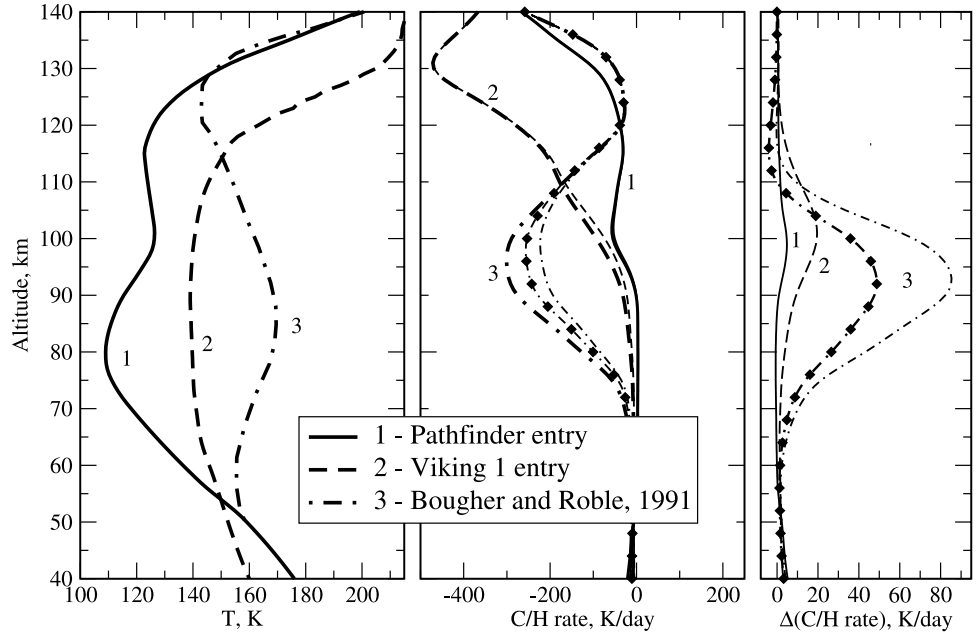

Figure 1. Comparison of the exact cooling rates due to the 15 μm CO_2 band with those computed with the scheme employed in the GCM. (left) Temperature profiles used for the comparison (see text). (middle) Total cooling/heating rates. Thick lines denote the exact calculations for the corresponding temperature profiles. Thin lines correspond to the calculations with the current scheme. The thin line with solid diamonds represents calculations with the extended scheme (see text). (right) Errors of the estimation of the cooling/heating rates by the scheme employed in the GCM (thin lines) and by the extended scheme (thin line with solid diamonds).

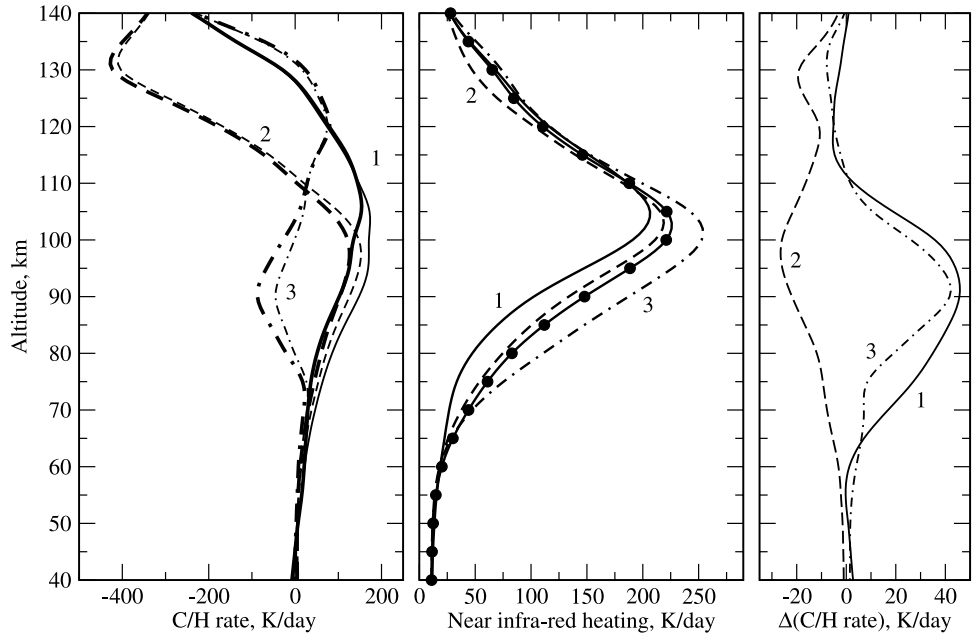

Figure 2. Same is in Figure 1 but for the daytime solar overhead conditions. (left) Total cooling/heating rates. Thick lines denote the exact calculations for the temperature profiles from the left panel in Figure 1; thin lines are for the calculations with the scheme implemented in the GCM. (middle) Heating rates caused by the absorption of the solar near infrared radiation. The solid line with solid circles corresponds to the parameterization of *Forget et al.* [1999]. (right) Errors of estimation of the total cooling/heating rates by the scheme applied in this work.

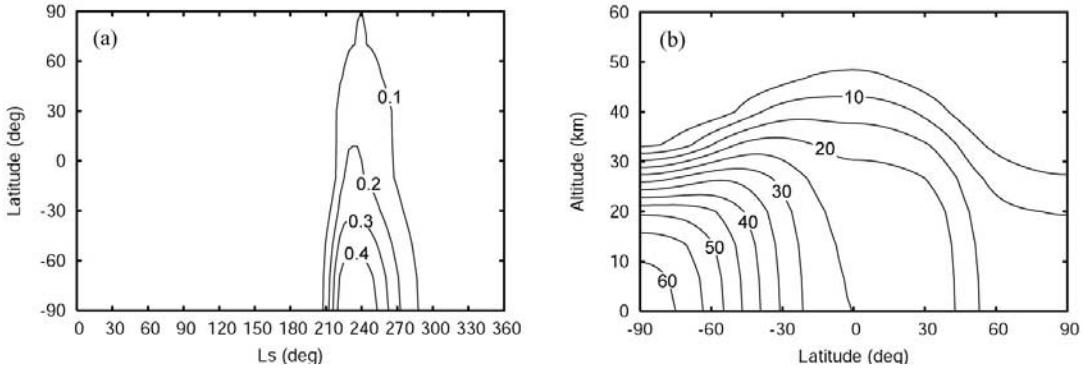

Figure 3. Dust scenario employed in the model: (a) Seasonal-latitudinal cross section of the visible (0.67 μm) dust opacity at 6 hPa. (b) Latitude-altitude cross section of the dust mass mixing ratio ($\times 10^7$) at $L_s = 270°$.

temperature profiles described in section 3.1. These heating rates are compared with the estimate from the parametric formula suggested by *Forget et al.* [1999]. In order to maintain the computational efficiency, and on the basis of the above satisfactory comparison, we utilize the formula from [*Forget et al.*, 1999] instead of the detailed calculations in the near-infrared for the estimate of the heating rates. The left panel of Figure 2 compares the total (day time) cooling/heating rates computed by the CO_2 radiation scheme employed in the GCM with those calculated in the line-by-line reference model. The corresponding errors are given in the right-hand panel of the same figure. They vary from −25 to +40 K day^{-1}.

3.3. Dust Radiation

[18] The absorption, emission and scattering by atmospheric dust are calculated using the two-stream formulation of the radiative transfer [*Meador and Weaver*, 1980] and employing the δ-Eddington approximation for the phase function [*Joseph et al.*, 1976]. The dust radiation is treated independently of the CO_2 radiation. Four representative wavelength bands are introduced between 0.1 and 200 μm to approximate the transfer in entire spectrum: two in the visible and two in the infrared spectral range. Effects of the dust in the CO_2 15 μm band are neglected. The optical parameters of the dust are taken from *Ockert-Bell et al.* [1997] for the visible and from *Forget* [1998] for the infrared. The particle size distribution is taken from [*Tomasko et al.*, 1999]. It represents a modified gamma function with the effective radius of 1.6 μm and the effective variance 0.2 μm. The dust opacity in the visible (0.67 μm) is set to be twice of that in the infrared (9 μm).

[19] The distribution of the dust varies with the aerocentric longitude and latitude. In our nominal scenario, it is set to be qualitatively consistent with the TES2 dust scenario of *Kuroda et al.* [2005]. Briefly, to account for the rapid increase of the dust opacity during a dust storm followed by the slower decay, we used the analytical formula for the dust opacity at 6 hPa, $\tau_i(L_s)$:

$$\begin{aligned}\tau_i(L_s) &= 0.05 + 0.5(\tau_{\max} - 0.05)[1 + \tanh[\alpha(L_s - L_{s0})] \\ &\quad \text{for } L_s < L_{s1}, \\ \tau_i(L_s) &= 0.05 + (\tau_{\max} - 0.05)\cos^{\beta}[0.5(L_s - L_{s1})] \\ &\quad \text{for } L_s \geq L_{s1}.\end{aligned} \tag{1}$$

τ_i (L_s) are calculated at the equator, South and North poles, as τ_{eq}, τ_S and τ_N, respectively. The values of $\tau_{\max}$, L_{s0}, L_{s1}, α and β in the above equations are given by the Table 1 of *Kuroda et al.* [2005]. The optical depth at all latitudes φ, $\tau(\phi, L_s)$, is then prescribed as follows:

$$\begin{aligned}\tau(\phi, L_s) &= \tau_N + 0.5(\tau_{eq} - \tau_N) \\ &\quad \times\{1 + \tanh[5(45° - \phi)]\}, \quad \phi > 0, \\ \tau(\phi, L_s) &= \tau_S + 0.5(\tau_{eq} - \tau_S) \\ &\quad \times\{1 + \sin[2(45° - \phi)]\}, \quad \phi < 0.\end{aligned} \tag{2}$$

Summarizing the above two distributions, Figure 3a presents the seasonal variation of the visible (0.67 μm) dust opacity at 6 hPa. For the vertical dust mixing ratio distribution, Q, we have chosen the function from *Forget et al.* [1999] and *Lewis et al.* [1999]:

$$\begin{aligned}Q &= Q_0 \exp\left\{0.007\left[1 - \left(\frac{p_0}{p}\right)^{70/z_{\max}}\right]\right\}, \\ z_{\max}(\phi, L_s) &= 60 + 18\sin(L_s - 160°) - 22\sin^2\phi.\end{aligned} \tag{3}$$

The latitude-altitude cross section of the dust mixing ratio for $L_s = 270°$ is shown in Figure 3b.

[20] To estimate the accuracy of the dust scheme employed in the model, we compared it with the one from the CCSR/NIES Martian AGCM [*Kuroda et al.*, 2005]. In the latter, 19 wavelength bands were introduced between 0.2 and 200 μm: 9 in the visible and 10 in the infrared. Figure 4 presents the profiles of the dust induced heating and cooling for the both schemes. They were calculated for the infrared (9 μm) dust opacity of 1.0, the vertical distribution as in (3) with $z_{\max}$ = 70 km. Dust heating tends to be lower in the 4-band scheme for lower zenith angles, and the heating rates are smaller at lower heights compared to the 19 band scheme. The cooling rate profiles are qualitatively consistent, although the magnitude in the 4-band scheme is weaker for higher atmospheric temperatures. Partially, this may compensate for the lower heating rates near the surface. The choice of the 4 spectral ranges in our calculations follows the compromise between the accuracy and the computer efficiency, and is in line with the dust schemes in other Martian GCMs [*Moudden and McConnell*, 2005].

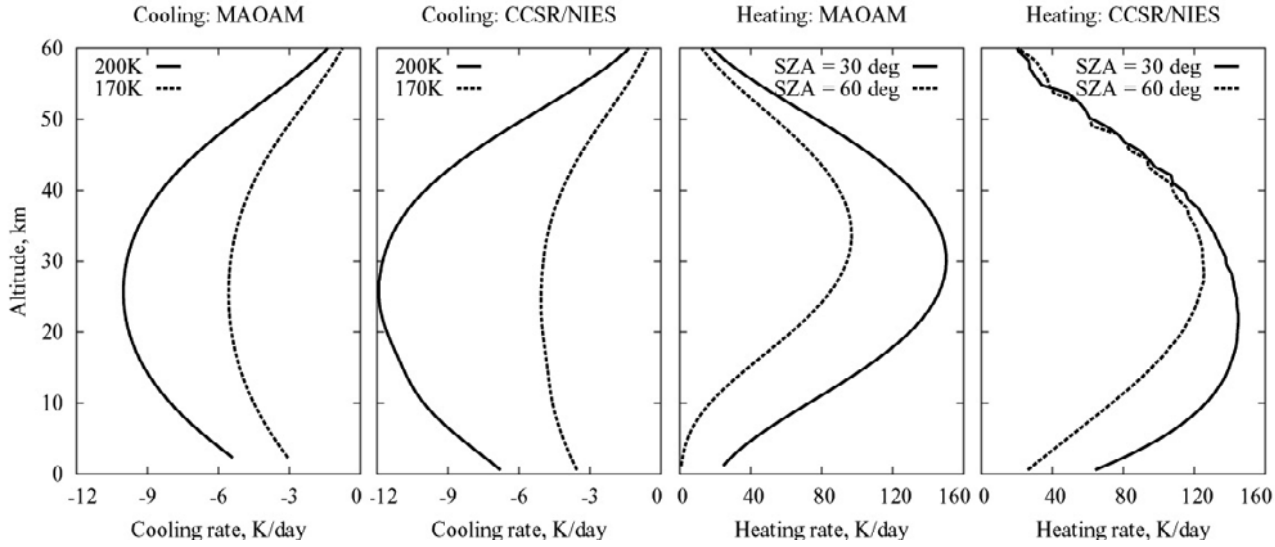

Figure 4. Comparison of the cooling and heating rates calculated with the 4-band dust radiative scheme employed in the model (titled MAOAM) with the 19-band scheme of *Kuroda et al.* [2005] (titled CCSR/NIES).

Note that the variations of the heating/cooling rates due to the uncertainties in the dust parameters exceed those due to the reduced number of spectral intervals.

4. Surface Energy Budget

[21] A slab model is used to determine the evolution of the surface temperature in the model [e.g., *Gierasch and Goody*, 1968; *Zhang and Anthes*, 1982]. The energy balance equation at the surface has the form

$$c_g \frac{dT_g}{dt} = F_{rad} - H_g + H_m, \tag{4}$$

where T_g is the temperature of the ground; F_{rad} is the net radiative flux (including the solar and thermal components); H_g is the sensible heat flux from the surface to the atmosphere; H_m is the heat flux into the soil. The latent heat flux is neglected in the present formulation. The thermal capacity of the slab, c_g, is related to the thermal inertia [*Blackadar*, 1979]. We use the surface thermal inertia map [*Mellon et al.*, 2000] measured by the Thermal Emission spectrometer (TES) on board the Mars Global Surveyor.

[22] The net radiative flux at the surface is the balance between the incoming and outgoing direct solar radiation (S) and the thermal (TH) radiative fluxes:

$$F_{rad} = F_S^{\downarrow} - F_S^{\uparrow} + F_{TH}^{\downarrow} - F_{TH}^{\uparrow}. \tag{5}$$

The solar radiation flux $F_S^{\downarrow}$ is computed from the black body emissivity of the Sun, the geometry of the orbit (day of the year), the solar zenith angle (local time), and the absorption and scattering by the atmospheric dust. The outgoing solar radiation is determined by the surface albedo, A: $F_S^{\uparrow} = \mathrm{A}F_S^{\downarrow}$. The thermal in- and outgoing radiative fluxes, $F_{TH}^{\downarrow} - F_{TH}^{\uparrow}$, are taken from the CO_2 and the dust radiation schemes. The surface albedo map [*Christensen et al.*, 2001] obtained from the TES observations is employed in our calculations.

[23] The heat fluxes into the ground are calculated from the equation

$$H_m = c_g K_m \left(T_g - T_m\right), \tag{6}$$

where the heat transfer coefficient K_m is proportional to the rotation frequency of the planet [*Zhang and Anthes*, 1982], T_m is the temperature of the soil underground which is set equal to the running zonal average of the surface temperature [*Pollack et al.*, 1981]. The sensible heat flux from the surface into the atmosphere due to both the molecular conduction and turbulent diffusion, H_g, is modeled after *Gierasch and Goody* [1968].

5. CO_2 Condensation and Sublimation

[24] Only thermal effects of CO_2 condensation and sublimation are considered in the model. When the temperature of the air or surface drops below the freezing point, condensation of CO_2 occurs, and the latent heat releases to keep the temperature from falling below. Sublimation is the reverse process, it works to maintain the freezing temperature if the ice is heated. The condensation temperature of CO_2 is calculated from the Clausius-Clapeyron relation [*Hourdin et al.*, 1995]. Mass effect of the atmospheric CO_2 condensation is ignored in this version of the model. *Haberle et al.* [1993] indicated that the change of mass of the Martian atmosphere affects little the zonal mean circulation. The latter is what we are mostly concerned with in this paper.

6. Subgrid-Scale Dynamics

6.1. Turbulent Diffusion

[25] The model employs a standard local diffusion parameterization for the free atmosphere based on the Richardson number with the parameters adapted from the terrestrial atmospheric NCAR–CAM3 (National Center for

Atmospheric Research–Community Atmospheric Model) GCM [*Holtslag and Boville*, 1993]. According to this approach, the turbulent fluxes of the wind velocity and potential temperature are proportional to their local gradients with the proportionality coefficients K_u and K_T, correspondingly. The vertical turbulent mixing of these field variables is expressed in terms of the vertical gradients of their turbulent fluxes. Dissipation of the kinetic energy results in the heating which is accounted for by the diffusive heating term:

$$\epsilon_{Diff} = c_p^{-1} K_u \left[\left(\frac{\partial u}{\partial z} \right)^2 + \left(\frac{\partial v}{\partial z} \right)^2 \right]. \quad (7)$$

The free atmospheric turbulent diffusivities are typically taken as functions of length scales l_c and local vertical gradients of wind and virtual potential temperature

$$K_c = l_c^2 S F_c(Ri), \quad (8)$$

where S is the local wind shear

$$S = \sqrt{\left(\frac{\partial u}{\partial z} \right)^2 + \left(\frac{\partial v}{\partial z} \right)^2}. \quad (9)$$

The mixing length is given by

$$l_c^{-1} = (k_c z)^{-1} + \lambda_c^{-1}, \quad (10)$$

where $k_c = 0.4$ is the von Karman constant, and λ_c is the asymptotic length scale set to 30 m, as in NCAR-CAM3 [*Holtslag and Boville*, 1993]. The stability function $F_c(Ri)$ gives the dependence of the turbulent diffusivity K_c on the Richardson number $Ri = g(S^2\theta)^{-1}(\partial\theta/\partial z)$, θ being the potential temperature. For simplicity, we make no distinction between the diffusivity coefficients for the wind velocity and temperature, $K_u = K_T = K_c$, and choose the following stability functions [*Holtslag and Boville*, 1993]:

$$\begin{aligned} F_c(Ri) &= (1 - 18Ri)^{1/2}, \qquad Ri < 0 \\ F_c(Ri) &= [1 + 10Ri(1 + 8Ri)]^{-1}, \qquad Ri \geq 0 \end{aligned} \quad (11)$$

Since the Martian boundary layer is significantly shallower than the vertical resolution of our model, the local diffusion approach represents a pretty good approximation in the free atmosphere. We rely on the calculated diffusivities in the entire model's domain.

6.2. Convective Adjustment and the Rayleigh Friction

[26] The parameterization described in the previous subsection reacts on the convectively unstable temperature profiles by the enhanced turbulent thermodiffusion coefficients. As in many other GCMs, the corresponding diffusion cannot alone describe the process of rapid mixing of heat within unstable layers. Therefore, to completely prevent superadiabatic lapse rates in the numerical solution, we employ a standard energy-conserving convective adjustment scheme. In the model, it is called after the turbulent diffusion scheme to restore the stability of the atmosphere by adjusting the temperature in the vertical column and keeping the potential temperature gradient positive, $d\theta/dz \geq 0$.

[27] Rayleigh friction is imposed near the top of the model. It imitates the missing damping effects in the upper atmosphere from the molecular viscosity and, perhaps, broad-spectrum gravity wave drag. The Rayleigh friction coefficient grows exponentially with height above 100 km and reaches 9 sol^{-1} at z = 130 km. The parameters of the coefficient were chosen in numerical experiments as a balance between the two requirements: the effect of the friction on the fields below 110 km must be as gentle as possible, while maintaining the stability of the model. Our Rayleigh friction coefficient is consistent with other atmospheric GCMs [e.g., *Takahashi et al.*, 2003].

6.3. Gravity Wave Drag Parameterization

[28] The impact of subgrid-scale gravity waves (GW) usually has to be parameterized. It is little known about the GW spectra and sources on Mars. The lack of wind measurements in the middle atmosphere provides little information about the effects of broad-spectrum GWs. Therefore we employ only the parameterization of effects of gravity waves excited by the subgrid-scale orography. The source magnitudes of GW harmonics with zero phase velocity above the resolved topography is estimated after *McFarlane* [1987]. At the lower boundary, the mean squared (averaged over the size of a grid) variation of the velocity fluctuations is then given by $\overline{u'^2} = \overline{h'^2} N^2/4$, where N is the Brunt-Vaisala frequency, and $\overline{h'^2}$ is the subgrid scale variance of the topography. The latter has been calculated from the high resolution Digital Elevation Map [*Delacourt et al.*, 2003] by subdividing the subgrid topography into M bins of the size of half the characteristic subgrid gravity wave length (100 km), and computing $\overline{h'^2} = M^{-1} \sum (h - \overline{h})^2$. h denotes the topography height within the bins, and $\overline{h}$ is the resolved topography. The direction of propagation of the wave is chosen along the mean wind at the source level.

[29] Once the source magnitude of the GW harmonic at the lower boundary is specified, the vertical propagation including effects of the refraction, nonlinearities, and ultimately breaking and dissipation near critical levels is calculated using the parameterization of *Medvedev and Klaassen* [2000]. According to this spectral scheme adapted for one harmonic, the vertical evolution of the wave amplitude u' is given by

$$\frac{d\overline{u'^2}}{dz} = \left(-\frac{1}{H} + \frac{m_z}{m} - \beta \right) \overline{u'^2}, \quad (12)$$

where $m = -N/\bar{u}$ is the vertical wavenumber, $\bar{u}$ is the projection of the local wind in the model onto the direction of the wind at the lower level; H is the scale height; $\beta = \sqrt{2\pi} N \exp(-\bar{u}^2/2\overline{u'^2})/\sqrt{\overline{u'^2}}$ is the nonlinear damping rate. The horizontal acceleration in the direction of the mean wind at the source level can then be calculated using

$$a_{GW} = m^{-1} k \beta \overline{u'^2}. \quad (13)$$

Heating and thermal diffusion coefficients induced by the breaking gravity waves are calculated according to *Medvedev and Klaassen* [2003]. The only tunable parameter in the scheme is the characteristic horizontal wavenumber

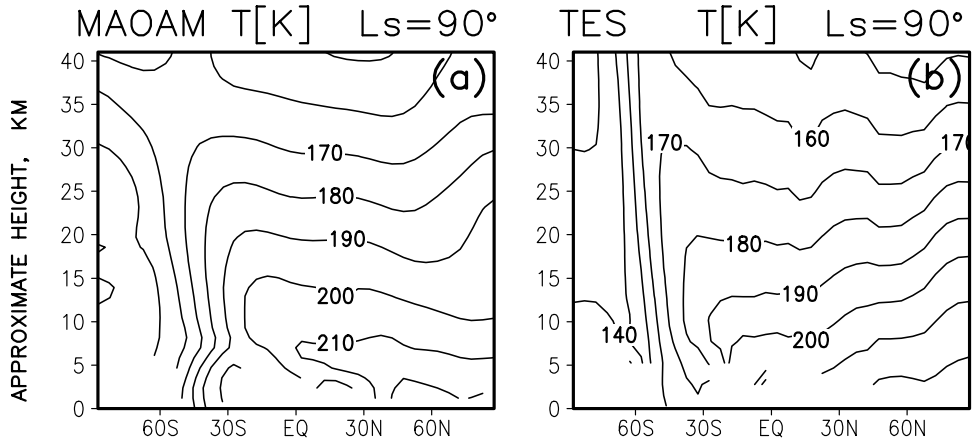

Figure 5. Zonal mean temperature for $L_s = 90°$ (a) simulated with the model and (b) obtained from the TES measurements. The contour interval is 10 K.

($k = 2\pi/\lambda$). We use $\lambda = 200$ km in the model, the middle value between the typical wavelengths 100 and 300 km employed in the terrestrial GCMs of the comparable horizontal resolution [*Medvedev and Klaassen*, 2000].

7. Zonal-Mean Climatology

[30] In this section we present the results of the numerical simulations employing the 32 × 36 grid point horizontal resolution. First, the model was spun up from the state of the rest and a globally uniform temperature $T = 160$ K. The spin-up was done for the perpetual solar longitude L_s = const, i.e., allowing only daily variations and keeping the solar zenith angle constant. After 10–15 sols, the model reaches a practically equilibrium state. This adjustment is significantly faster than that for the terrestrial conditions because of the smaller mass of the Martian atmosphere. Then, the model was run with L_s allowed to increase. The results referred below to a particular season (or L_s) are in fact the average over the interval $[L_s - 3°, L_s + 3°]$. This interval is comparable with the length of temporal averaging for the zonal mean climatology from TES [*Smith et al.*, 2001]. The removal of the transience allows one to consider the fields as to some degree a "seasonal" mean corresponding to a particular L_s. The dust scenario is described in section 3.3. The dust optical depth in the visible at the equator is 0.18 for $L_s = 270°$.

7.1. Northern Summer Solstice, $L_s = 90°$

[31] The only global measurements of the zonally averaged temperature of the Martian atmosphere available to us were taken from the Thermal Emission Spectrometer (TES) on board the MGS [*Smith et al.*, 2001]. Figure 5 presents the comparison between the temperature deduced from the nadir measurements by TES (the right panel) and the corresponding vertical domain of the simulated zonal mean temperature (the left panel). The figure shows an overall agreement in magnitudes and patterns of the temperature fields. The discrepancies near the surface may partly arise due to differences in the zonal averaging procedures for temperature in the model and observations. At the lower atmospheric levels in the presence of topography (but not on the surface), the averaging in the model is done over only those grid points on a latitude circle that lie above the surface. This was followed by the temporal averaging over $\Delta L_s = 6°$, as described above. In the Southern hemisphere, the model successfully captures CO_2 freezing surface temperatures up to approximately 60°S, the strong meridional gradients in midlatitudes, and the polar minimum.

[32] The simulated zonally averaged temperature and zonal wind are shown in Figure 6 up to 110 km. Note that the real domain of integration goes up to 130 km, but its upper portion is contaminated by the waves reflected from the model's lid, and is used here for numerical stability purposes only. One feature which stands out quite clearly is the strong winter polar temperature inversion, and the corresponding strong polar warming centered around 60–70 km. This southern winter polar warming has been observed [*Deming et al.*, 1986] and reproduced in GCMs, however, with a lower magnitude than in our simulations [*Forget et al.*, 1999]. Note that this warming was weaker in our earlier experiments with the LTE only CO_2 15 μm radiation scheme, although still somewhat stronger than in *Forget et al.* [1999]. Turning on the non-LTE capabilities of the scheme reduces the cooling rates compared to the one produced by the pure LTE parameterization, and therefore results in the overall increase of atmospheric temperatures. In line with other Martian GCMs, the minimum of temperature appears over the equatorial region between 60 and 70 km, but its magnitude of slightly less than 130 K is about 10 to 20 K colder than reported by *Forget et al.* [1999] and *Moudden and McConnell* [2005]. The zonal mean wind cross section in Figure 6b demonstrates the strongly tilted westerly polar night jet with the magnitude of above 70 m s^{-1}. This is lower than estimated from the TES measurements [*Smith et al.*, 2001]; however, direct wind measurements do not yet exist. Instantaneous values of the zonal wind above 70 km may exceed 200 m s^{-1} when longitudinal variations associated with tides and planetary waves superimpose the mean flow. In the summer (Northern) hemisphere, the weak westerlies extend up to almost 40 km. Unlike in the Earth, the easterlies extend deep into the winter hemisphere, and cover it entirely above 90 km.

[33] The origin of the winter polar warming in the Martian atmosphere has been extensively discussed [see *Wilson*, 1997; *Forget et al.*, 1999; and references therein]. It

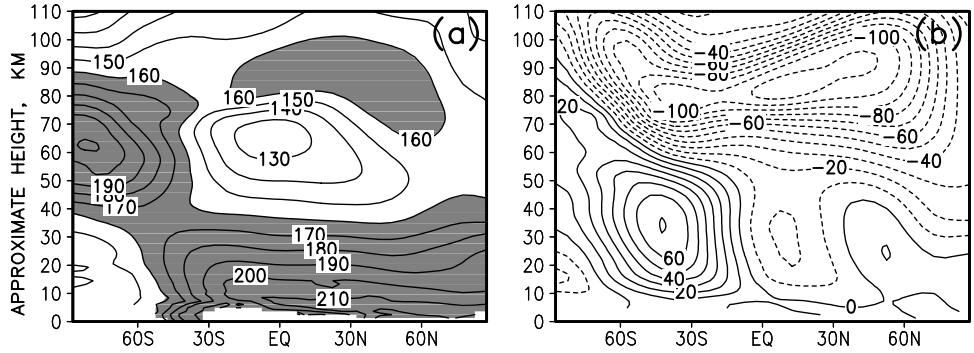

Figure 6. (a) Zonally averaged temperature and (b) zonal wind simulated for $L_s = 90°$. The shaded area in Figure 6a denotes the temperatures above 160 K.

has been correctly related to the strength and shape of the global Hadley cell, which, in turn, is controlled by the differential diabatic heating and interactions of the mean flow with zonally asymmetric eddies (planetary and gravity waves, tides). *Wilson* [1997] stressed the role of the diabatic heating in the formation of the winter polar warming at $L_s = 270°$. Here we consider the effect of eddies in forcing the warming in more detail. This effect enters the mean zonal momentum equation in the Transformed Eulerian Mean (TEM) formulation through the divergence of the Eliassen-Palm (EP) fluxes [*Andrews et al.*, 1987]:

$$\bar{u}_t + \bar{v}^*\left[(a\cos\phi)^{-1}(\bar{u}\cos\phi)_\phi - f\right] + \bar{w}^*\bar{u}_z = (\rho_0 a\cos\phi)^{-1}\nabla\cdot\mathbf{F}. \quad (14)$$

In (14), $\bar{v}^*$ and $\bar{w}^*$ are the residual velocities defined as $\bar{v}^* = \bar{v} - \rho_0^{-1}(\rho_0 v'\theta'/\bar{\theta}_z)_z$ and $\bar{w}^* = \bar{w} + (a\cos\phi)^{-1}(\cos\phi v'\theta'/\bar{\theta}_z)_\phi$; ϕ is the latitude, f is the Coriolis parameter, and $\mathbf{F}$ is the EP flux. The EP flux divergence is plotted in Figure 7a. Comparison with Figure 6b shows that the resolved eddies mostly tend to drag the mean zonal flow, although they do accelerate winter westerlies in the lower atmosphere, and summer easterlies in the upper Northern hemisphere. The maximum of the EP flux divergence is in the winter hemisphere. The contribution of the parameterized orographic gravity waves (not shown here) is concentrated in this region too, but almost an order of magnitude (few tens m s^{-1} sol^{-1}) weaker. To show the induced meridional transport, we plotted the stream lines of the residual circulation in Figure 7c. The residual velocities take into

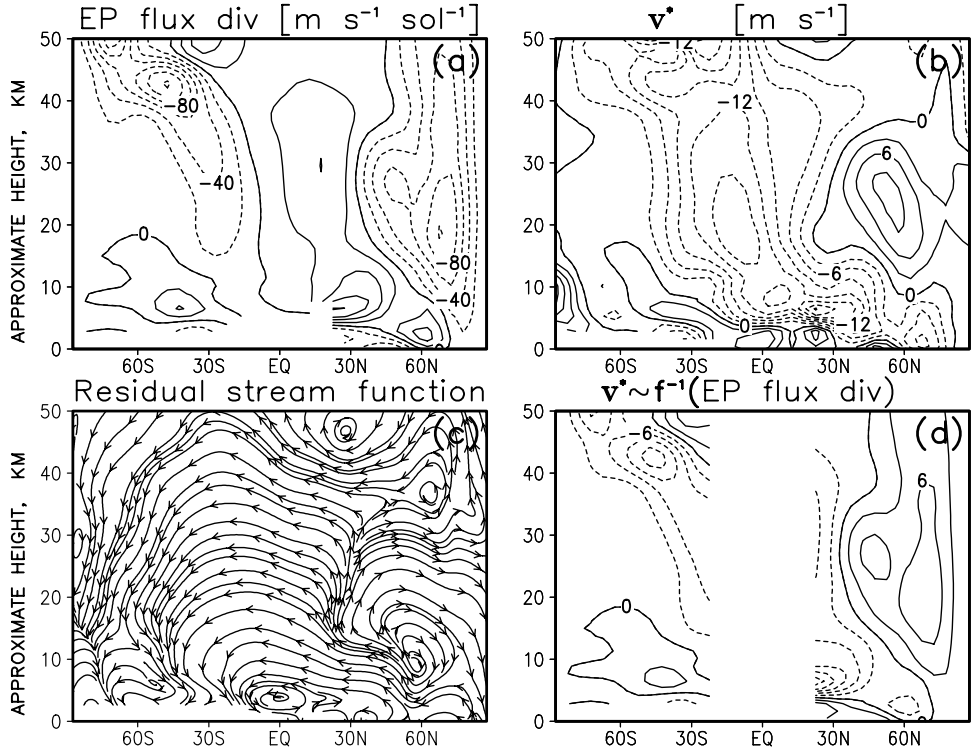

Figure 7. The fields simulated for the solar longitude $L_s = 90°$: (a) Eliassen-Palm flux divergence. The contour interval is 100 m s^{-1} sol^{-1}. (b) The residual meridional velocity $\bar{v}^*$. (c) The residual stream function. (d) The estimate of the meridional residual velocity from (14): $\bar{v}^* \approx -f^{-1}(\rho_0 a\cos\phi)^{-1}\nabla\cdot\mathbf{F}$.

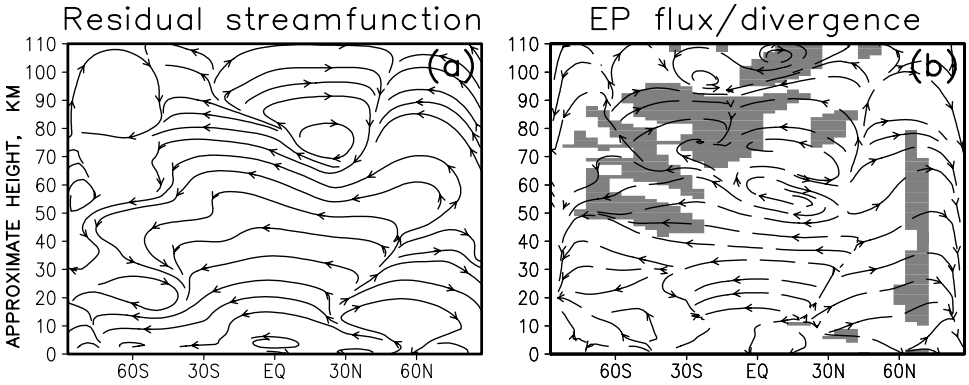

Figure 8. The fields simulated for $L_s = 90°$: (a) The stream lines of the residual circulation. (b) Stream lines of the Eliassen-Palm fluxes due to the resolved eddies (long dashed lines), and the corresponding divergence of these fluxes (shaded areas). Only divergences stronger than 30 m s^{-1} sol^{-1} in absolute value are shown.

account the transport by eddies, and represent the net transport closer than the Eulerian counterparts [*Andrews et al.*, 1987]. Figure 7c demonstrates the rising motions in midlatitudes of the summer hemisphere, cross-equatorial transport, and the descend over the winter pole. The smaller poleward circulation cell in the summer hemisphere forces the westerlies below 60 km. The meridional component of the residual velocity $\bar{v}^*$ is shown in Figure 7b. Its magnitude of several tens m s^{-1} is significantly stronger than that on the Earth, and is in line with the results from other Martian GCMs. The transience in (14) can be neglected for the seasonal average. Therefore $\bar{v}^*$ may be determined from (14) from the EP flux divergence and the advection. Figure 7d presents the estimate for $\bar{v}^*$ calculated using the eddy forcing from the panel 7a, and the Coriolis term: $\bar{v}^* \approx (\rho_0 af \cos\phi)^{-1} \nabla \cdot \mathbf{F}$. Comparison with the Figure 7b shows that the residual meridional velocity $\bar{v}^*$ is determined largely by the EP flux divergence (at least in midlatitudes to high latitudes). In other words, the meridional transport is forced primarily by the eddies, and the peculiarities of this forcing control the winter polar warming.

[34] A useful diagnostics for highlighting the origination and propagation of eddies is their EP flux, or the flux of wave action. In Figure 8b, we plotted with the bold dashed lines the calculated EP fluxes together with their divergence denoted by the thin lines. The corresponding residual circulation in the entire domain of integration is given in Figure 8a. The inspection of this figure shows that the strong EP flux divergence occurs in the winter hemisphere around the location of the winter polar temperature maximum. The waves affecting the circulation there propagate mainly from the two directions: from below, and horizontally from the midlatitudes of the summer hemisphere. The former waves are most likely generated by the flow over the topography, and by the diurnal temperature variations on the surface. The latter waves are the tidal and planetary wave harmonics in situ excited by the strong diurnal variations of heating. Above 80 km, the strong EP flux divergences are created by waves generated in the middle and upper atmosphere. Their trajectories are long and affected by a refraction. Overall it is seen, that the model produces the two distinct circulation cells: the summer-to-winter global transport below 70–80 km which is reported by most of the Martian GCMs, and the meridional cell in the opposite direction above. Direct measurements above 80 km are required to find out whether this upper cell does really exist.

[35] To further demonstrate the role of eddies, we have run the model with the surface topography set to zero. Thus the excitation of planetary waves on the lower boundary was significantly decreased, if not completely turned off. At the same time, the generation of thermal tides by the diurnal solar flux variations remained virtually unaffected. The results are shown in Figure 9, and demonstrate a drastic change in the simulated fields. Although the polar warming still appears in this experiment, it is almost 40 K colder than in the run with the full topography. The EP fluxes associated with the non-zonal disturbances are almost 10 times weaker, the same is for their divergence. The residual circulation (shown in Figure 9a by the stream lines) is then very close to the Eulerian one. As the result of this circulation, the wind distribution is more symmetric with respect to the Equator. The winter westerly jet is not tilted as much as in Figure 6b, and the summer easterlies are more confined to the summer hemisphere, and go all the way down to the surface.

7.2. Northern Fall Equinox, $L_s = 180°$

[36] Since the meridional gradients of the diabatic heating/cooling rates are weaker at equinoxes, the circulation is less robust. *Forget et al.* [1999] pointed out the sensitivity of the simulated equinox circulation patterns to the dynamical core of the model, or, ultimately, to the ability of the model to resolve the eddies. The results of our simulations for $L_s = 180°$ are compared with the TES temperature measurements in Figure 10. A very good agreement in zonal mean temperatures is seen in almost the entire domain except over the poles. In the low and midlatitudes, the difference hardly exceeds the errors associated with the TES [*Smith et al.*, 2001], while on the poles, it is around 10–15 K. Note that the maximum of temperatures in the low latitudes occurs not on the ground but about 10 km higher. Similar features are seen at some temperature profiles retrieved by radio occultation from MGS [*Hinson et al.*, 1999].

[37] The simulated zonal mean temperature and zonal wind are plotted in Figures 11a and 11b), correspondingly.

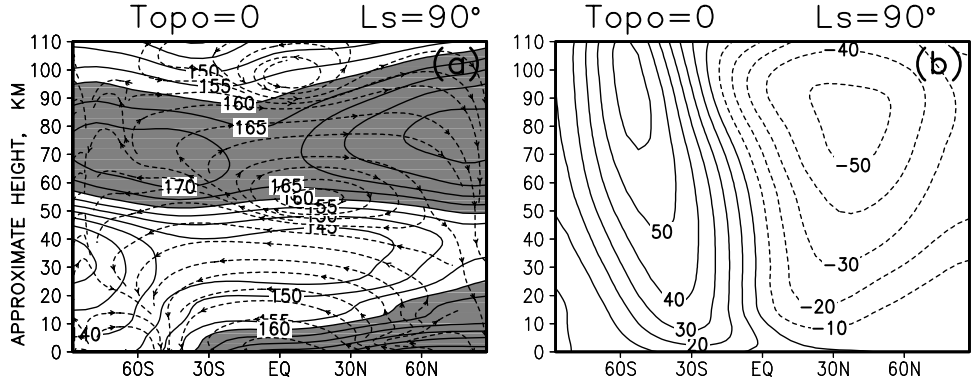

Figure 9. Results of the run with the topography turned off. (a) The mean zonal temperature (continuous lines), and the residual stream function (dashed lines with arrows). Shaded is the temperature above 160 K, as in Figure 6b). (b) Mean zonal wind.

The model reproduces the temperature maximums over the poles, however, warmer than in the TES limb measurements (below 60 km) and in the other models [*Forget et al.*, 1999; *Kuroda et al.*, 2005]. The simulated zonal mean wind exhibits two westerly jets below 60 km, and a strong easterlies (up to 170 m s^{-1}) covering the globe from the pole to pole. The westerly jets have about the same magnitude as in *Kuroda et al.* [2005], but slower than in *Forget et al.* [1999] (note that averages over a significantly longer time interval are reported in the latter paper). The EP flux divergence due to resolved eddies presented in Figure 11d is weaker than for the solstices. It generally imposes a deceleration on the wind, but the tendency to accelerate the easterlies in low latitudes above 50 km is clearly seen. Finally, the residual stream function is shown in Figure 11c. In the lower atmosphere, the model produces two transport cells in each hemisphere with rising motions in midlatitudes, and descending ones over the poles and the equator. Higher, mainly a pole to pole transport is seen with an additional cells near the warm polar regions.

[38] As in the case for the solstice L_s = 90°, topographically induced eddies control the circulation to a large degree. With the topography set to zero, the model produces practically symmetric distributions of the wind and temperature with respect to the equator (not shown here). This simulated temperature is almost 30 K colder below 40 km, and 10 to 15 K colder over the poles around 60 km. The temperature in the low latitudes above 60 km and throughout the globe above 80 km is practically unaffected. This may be an indication that only in situ generated tidal and planetary wave oscillations play a role in the interactions with the mean zonal fields. The corresponding zonal wind is weaker, westerlies extend to the top of the model domain, and the easterlies above 60 km occupy only low latitudes.

7.3. Northern Winter Solstice, L_s = 270°

[39] Due to the eccentricity of the Martian orbit, the meridional gradients of the CO_2 radiative heating/cooling rates are stronger during this time. Dust storms occur at and around this season too, therefore radiative effects of the dust are significantly enhanced. Compared to the CO_2 radiation scheme which is pretty good constrained (except for the CO_2 + O collisional quenching rate), the dust radiation parameterization is subjected to many uncertainties in the aerosol distribution and properties. Figure 12 shows the zonal mean temperature simulated (Figure 12a) and observed (Figure 12b) with TES. The dust optical depth in the visible was taken at 0.18 on the equator. This is compatible or somewhat lower than in the observations outside the dust storm seasons [*Liu et al.*, 2003, Figure 10]. It is also consistent with some other Martian GCMs: τ = 0 in [*Takahashi et al.*, 2003], τ = 0.2 in the NASA Ames MGCM [*Joshi et al.*, 2000], τ = 0.3 in [*Moudden and McConell*, 2005]. Some Martian GCM use even higher

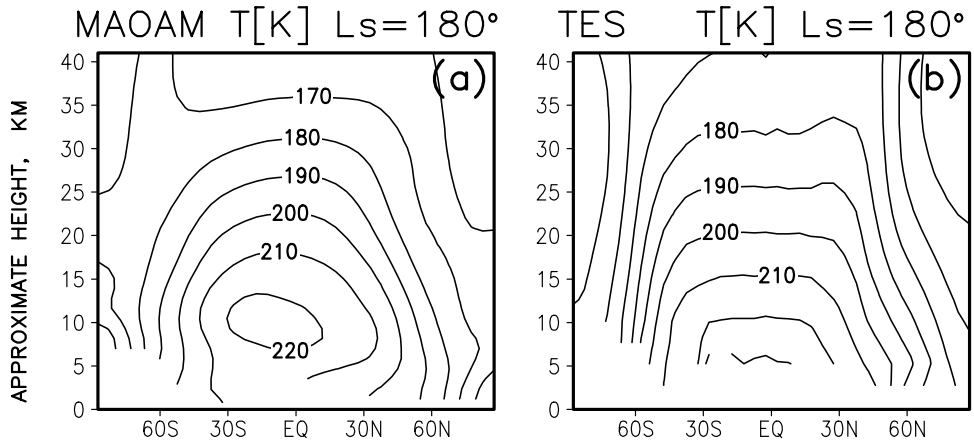

Figure 10. The same is in Figure 5 but for L_s = 180°.

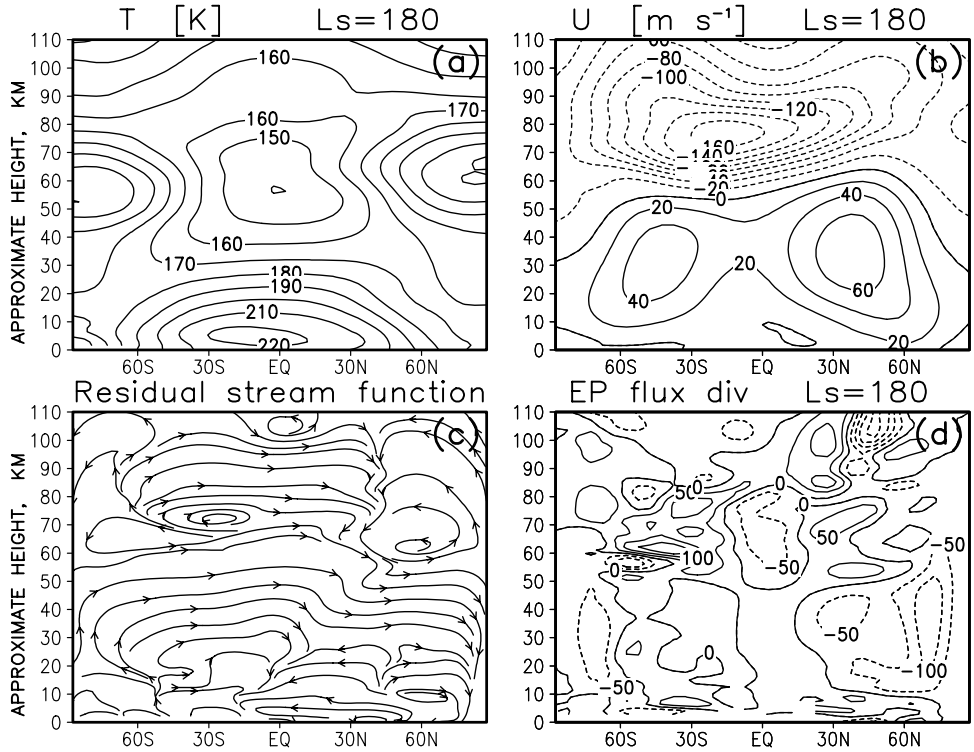

Figure 11. Zonal mean fields simulated for the solar longitude L_s = 180°: (a) temperature, (b) zonal wind, (c) residual stream function, and (d) EP flux divergence in m s^{-1} sol^{-1}.

amounts of dust, for example, τ = 1.0 at L_s = 270° in *Forget et al.* [1999] and τ = 6.0 in *Wilson* [1997]. In the latter paper, however, it is explicitly acknowledged that the simulations were performed for the dust storm conditions rather than for the mean climatological ones. In our simulations with higher dust opacities, we find that the atmospheric temperatures below 40 km become colder compared to the TES observations. The temperature above 40 km depends very little on the amount of dust. Note, that the temporal dependence of the dust optical depth used in all our experiments is shown in Figure 3a. This means that the simulations for the other seasons (both the reported and not shown here) were done with very small amount of dust (τ = 0.05).

[40] Figure 13 displays the simulated zonal mean temperature and wind in the full model domain up to 110 km. The wind and temperature patterns are similar to the ones at L_s = 90°, although somewhat amplified. Near the surface, the region with the strong temperature gradients is shifted equatorward compared to the observations. The winter polar warming at 60 km peaks at 240 K (compared to 210 K at L_S = 90°). The midlatitude temperature minimum of 150 K is almost 20 K warmer, and the midlatitude temperature maximum in the mesosphere just above is almost 40 K warmer than during L_s = 90°. The westerly jet at L_s = 270° is about 10 m s^{-1} stronger than in the other solstice, while the magnitude of the easterly jet at L_s = 270° is almost 50 m s^{-1} larger. Eddies are also stronger during

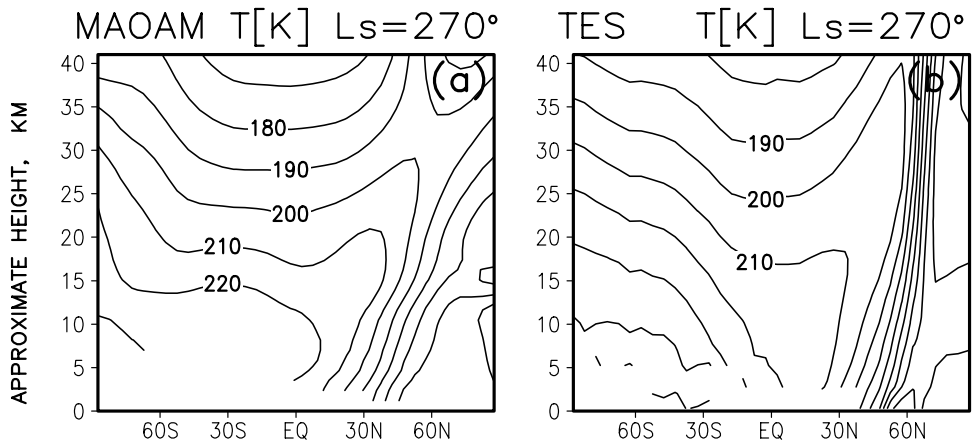

Figure 12. The same is in Figure 5 but for L_s = 270°.

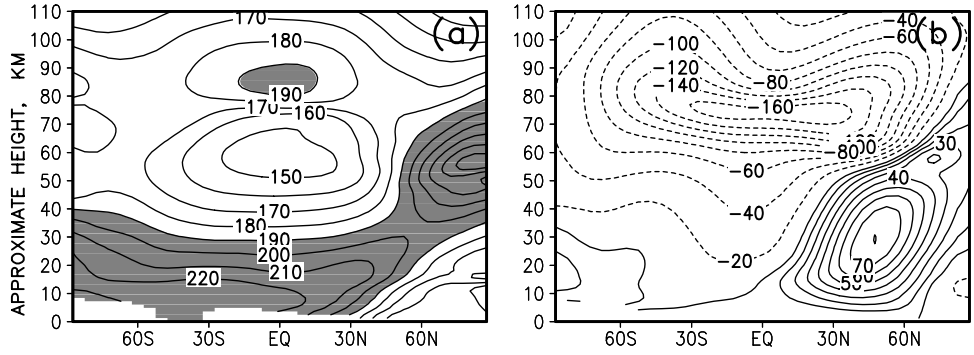

Figure 13. (a) Zonally averaged temperature and (b) zonal wind simulated for $L_s = 270°$. The shaded area in Figure 13a denotes the temperatures above 190 K.

the Northern winter solstice. Their EP fluxes as well as the corresponding EP flux divergences are the strongest in the entire Martian year. The impact of topographically generated waves was also studied, and is qualitatively similar to the one described in section 7.1.

8. Discussion

[41] Results of simulations with other Martian GCMs suggest that the upper atmosphere of Mars is highly sensitive to details of the dynamical core and other factors which affect the interactions of the eddies with the mean flow in the model [*Forget et al.*, 1999]. We have performed a series of numerical tests to ensure the internal validity of our model, and to study its sensitivity to the variation of some key parameters. In this section we give a summary of these experiments along with the general discussion of their results.

[42] The first line of experiments was related to the modifications in the dynamical core compared to the terrestrial version of COMMA–IAP. These changes were listed in section 2. The motivations for the changes were the following: allowing for the development of the natural variability in the model, reducing the numerical viscosity and damping, the energy and potential vorticity conservation, maintaining the stability for Martian conditions. At this stage, all the modifications were tested against the benchmark COMMA–IAP model.

[43] The second line of experiments included testing the physical parameterizations offline. We provide either short outlines of the sensitivity tests and the associated errors together with the description of these schemes (e.g., CO_2 15 μm radiation, the dust scheme), or the corresponding references (e.g., turbulent diffusion, gravity wave drag scheme).

[44] In the third line of tests, we studied the sensitivity of the model to the horizontal and vertical resolution and to the degree of the topography smoothing; the effects introduced by the non-LTE radiation and by the dust radiation with different dust opacities. A particular attention was paid to the robustness of the simulated patterns. We found that the latter strongly decreases when the horizontal resolution gets poorer. For example, if the grid step exceeds approximately 20 degrees in the longitudinal direction, the model produces almost pure zonal flow for the solstices with the jet streams extending into the upper atmosphere. The corresponding temperature reveals no winter polar warming in that case. Similar result can be obtained with higher horizontal resolution but artificially applying a strong non-zonal Newtonian cooling to inhibit the eddies in the model. Smoothing the topography results in weaker stationary planetary wave generation by the flow over the surface and thus to a weaker meridional circulation. The extreme case with the topography turned off is shown in section 7.1.

[45] However, the eddy forcing alone does not define the large scale circulation of the Martian atmosphere. We ran a series of tests with the LTE CO_2 15 μm radiation. The general effect was an increase of the radiative damping, as the LTE provides stronger atmospheric cooling. The winter polar warming in this case is 10 to 30 K colder, thus being more in line with simulations in other Martian GCMs. Our tests show a pretty weak sensitivity of the zonal mean fields below 100 km to the parameters of the sponge layer near the top of the model's domain. In part, this is explained by the high enough model lid. Shifting the onset of the sponge layer downward (e.g., as in *Kuroda et al.* [2005]) results in the effect somewhat similar to the LTE-only radiative cooling: a weaker meridional transport and therefore a weaker polar warming.

[46] Finally, our numerical experiments for different dust optical depths have shown high sensitivity of the model response in the lower atmosphere. The response in the zonal mean fields above approximately 50 km was limited.

9. Conclusion and Summary

[47] We present a new global general circulation model for the Martian atmosphere extending from the surface up to 130 km. The grid point model consists of a decisively re-designed dynamical core of the terrestrial Cologne Model of the Middle Atmosphere–Institute of Atmospheric Physics (COMMA–IAP), and a comprehensive set of physical parameterizations relevant to Mars. In particular, two novel parameterizations are included: (1) a highly accelerated version of the exact radiative non-LTE code for the 15 μm CO_2 bands and (2) a version of a spectral gravity wave drag scheme coupled for the first time with orographic gravity wave sources.

[48] The performance of the model is demonstrated with the zonal mean fields produced for different seasons. The simulated temperature is in a very good agreement with the TES measurements, the presently only available to us global observational data below 40 km. This encouraging ability of the model to reproduce the measured fields provides a hope

that it can adequately describe the atmosphere above 40 km as well. However, we must admit that the uncertainty in physical parameters required by the parameterization schemes for the upper portion of the Martian atmosphere, as well as a lack of observational data to compare with leaves us to some degree cautious.

[49] We used the model to demonstrate the role of resolved eddies in maintaining the circulation, and, in particular, in creating the winter polar warming. It follows from our numerical experiments, that the meridional transport, at least below 50–70 km, is primarily forced by the resolved thermal tide and planetary waves. Two types of waves affect the the zonally averaged circulation: those generated by the flow over the topography, and those excited in the atmosphere by the diurnally varying diabatic sources. Smoothing over the topography, or decreasing its resolution worsens the ability of the numerical model to resolve planetary wave generation, and, in turn, to reproduce the circulation properly.

[50] One physical mechanism which, if included, can significantly alter the results in the upper atmosphere is the gravity wave drag produced by a broad spectrum of subgrid scale GWs. These waves play an important role in the terrestrial atmosphere. The vertically stratified Martian atmosphere is convectively stable, therefore GWs of different scales can exist. Instabilities associated with strong wind shears can provide an ample source of GWs of various phase speeds. Thus broad spectrum "non-orographic" GW drag parameterizations may have to be necessarily included. However, the lack of observational data does not allow us to constrain GW drag schemes at this point. Therefore we limited the spectrum by the only "orographic" waves, the source of which can be specified very accurately from the topography. We found that the corresponding GW drag adds to the EP flux divergence due to the resolved eddies in forcing the meridional transport and enhancing the winter polar warming, although it is approximately 10 times weaker. The corresponding temperature maximum is about 5 K warmer with GWs than without them.

[51] Another uncertainty in high altitudes is related to the spatial distribution of the atomic oxygen. Cooling in the 15 μm CO_2 band is proportional to the O mixing ratio. Presently, we employ a globally averaged profile which may appear not to be exactly correct. Further observational data and/or coupling with interactive chemistry models are required.

[52] **Acknowledgment.** This work was supported by Deutsche Forschungsgemeinschaft, project HA 3261/1-2, and BMBF ("Deklim").

References

Andrews, D. G., J. R. Holton, and C. B. Leovy (1987), *Middle Atmosphere Dynamics*, Elsevier, New York.

Asselin, R. (1972), Frequency filter for time integration, *Mon. Weather Rev.*, *100*, 487–490.

Berger, U., and M. Dameris (1993), Cooling of the upper atmosphere due to CO_2 increases: A model study, *Ann. Geophys.*, *11*, 806–819.

Berger, U., and U. von Zahn (1999), The two-level structure of the mesopause: A model study, *J. Geophys. Res.*, *104*, 22,083–22,093.

Blackadar, A. K. (1979), High resolution models of the planetary boundary layer, *Adv. Environ. Sci. Eng.*, *1*(1), 50–80.

Bougher, S. W., and R. G. Roble (1991), Comparative terrestrial planet thermospheres: 1. Solar-cycle variation of global mean temperatures, *J. Geophys. Res.*, *96*, 11,045–11,055.

Christensen, P. R., et al. (2001), Mars Global Surveyor Thermal Emission Spectrometer experiment: Investigation description and surface science results, *J. Geophys. Res.*, *106*(E10), 23,823–23,872.

Delacourt, C., N. Gros, P. Allemand, and D. Baratoux (2003), Online Mars digital elevation model derived from MOLA profiles, *Eos Trans. AGU*, *84*(52), 583.

Deming, D., M. J. Mumma, F. Espenal, T. Kostiuk, and D. Zipoy (1986), Polar warming in the middle atmosphere of Mars, *Icarus*, *66*, 366–379.

Ebel, A., and U. Berger (1997), Martian atmosphere—Circulation and climate, final report, MART ACC, Bundesminist. für Bildung und Forsch., Berlin.

Forget, F. (1998), Improved optical properties if the Martian atmospheric dust for radiative transfer calculations in the infrared, *Geophys. Res. Lett.*, *25*, 1105–1108.

Forget, F., F. Hourdin, R. Fournier, C. Hourdin, O. Talagrand, M. Collins, S. R. Lewis, P. L. Read, and J.-P. Huot (1999), Improved general circulation models of the Martian atmosphere from the surface to above 80 km, *J. Geophys. Res.*, *104*, 24,155–24,175.

Gierasch, P., and R. Goody (1968), A study of the thermal and dynamical structure of the Martian lower atmosphere, *Planet. Space. Sci.*, *16*, 615–646.

Gusev, O. A., and A. A. Kutepov (2003), Non-LTE gas in planetary atmospheres, in *Stellar Atmosphere Modeling*, edited by I. Hubeny, D. Mihalas, and K. Werner, *ASP Conf. Ser.*, *288*, 318–330.

Haberle, R. M., J. B. Pollack, J. R. Barnes, R. W. Zurek, C. B. Leovy, J. R. Murphy, H. Lee, and J. Schaeffer (1993), Mars atmospheric dynamics as simulated by NASA Ames general circulation model: 1. The zonal-mean circulation, *J. Geophys. Res.*, *98*, 3093–3123.

Hinson, D. P., R. A. Simpson, J. D. Twicken, G. L. Tyler, and F. M. Flasar (1999), Initial results from radio occultation measurements with Mars Global Surveyor, *J. Geophys. Res.*, *104*(E11), 26,997–27,012.

Holtslag, A. A. M., and B. A. Boville (1993), Local versus nonlocal boundary-layer diffusion in a global climate model, *J. Clim.*, *6*, 1825–1842.

Hourdin, F., F. Forget, and O. Talagrand (1995), The sensitivity of the Martian surface pressure and atmospheric mass budget to various parameters: A comparison between numerical simulations and Viking observations, *J. Geophys. Res.*, *100*, 5501–5523.

Jakobs, H. J., M. Bischof, A. Ebel, and P. Speth (1986), Simulation of gravity wave effects under solstice conditions using a 3-D circulation model of the middle atmosphere, *J. Atmos. Terr. Phys.*, *48*, 1203–1223.

Joseph, J. H., W. J. Wiscombe, and J. A. Weinman (1976), The Delta-Eddington approximation for radiative flux transfer, *J. Atmos. Sci.*, *33*, 2452–2459.

Joshi, M., R. Haberle, J. Hollingsworth, and D. Hinson (2000), A comparison of MGS Phase 1 aerobraking radio occultation data and the NASA Ames Mars GCM, *J. Geophys. Res.*, *105*, 17,601–17,615.

Kuroda, T., N. Hashimoto, D. Sakai, and M. Takahashi (2005), Simulation of the Martian atmosphere using a CCSR/NIES AGCM, *J. Meteorol. Soc. Jpn.*, *83*, 1–19.

Kutepov, A. A., O. A. Gusev, and V. P. Ogibalov (1998), Solution of the non-LTE problem for molecular gas in planetary atmospheres: Superiority of accelerated lambda iteration, *J. Quant. Spectrosc. Radiat. Transfer*, *60*, 199–220.

Leovy, C., and Y. Mintz (1969), Numerical simulation of the atmospheric circulation and climate of Mars, *J. Atmos. Sci.*, *26*, 1167–1190.

Lewis, S. R., M. Collins, P. L. Read, F. Forget, F. Hourdin, R. Fournier, C. Hourdin, O. Talagrand, and J.-P. Huot (1999), A climate database for Mars, *J. Geophys. Res.*, *104*, 24,177–24,194.

Liu, J., M. I. Richardson, and R. J. Wilson (2003), An assessment of the global, seasonal, and interannual spacecraft record of Martian climate in the thermal infrared, *J. Geophys. Res.*, *108*(E8), 5089, doi:10.1029/2002JE001921.

López-Puertas, M., and M. López-Valverde (1995), Radiative energy balance of $CO_2$2 non-LTE infrared emissions in the Martian atmosphere, *Icarus*, *114*, 113–129.

López-Valverde, M., and M. López-Puertas (2001), Technical report: CO_2 non-LTE cooling rate at 15-μm and its parameterization for the Mars atmosphere, *ESA 11369/95/NL/JG CCN2*, Eur. Space Agency, Paris.

McFarlane, N. A. (1987), The effect of orographically excited gravity wave drag on the general circulation of the lower stratosphere and troposphere, *J. Atmos. Sci.*, *44*, 1775–1800.

Meador, W. E., and W. R. Weaver (1980), Two-stream approximations to radiative transfer in planetary atmospheres: A unified description of existing methods and a new improvement, *J. Atmos. Sci.*, *37*, 630–643.

Medvedev, A. S., and G. P. Klaassen (2000), Parameterization of gravity wave momentum deposition based on a nonlinear theory of wave spectra, *J. Atmos. Sol. Terr. Phys.*, *62*, 1015–1033.

Medvedev, A. S., and G. P. Klaassen (2003), Thermal effects of saturating gravity waves in the atmosphere, *J. Geophys. Res.*, *108*(D2), 4040, doi:10.1029/2002JD002504.

Mellon, M. T., B. M. Jakosky, H. H. Kieffer, and P. R. Christensen (2000), High resolution thermal inertia mapping from the Mars Global Surveyor Thermal Emission Spectrometer, *Icarus*, *148*, 437–455.

Mihalas, D. (1978), *Stellar Atmospheres*, 2nd ed., 632 pp., W. H. Freeman, New York.

Moudden, Y., and J. C. McConnell (2005), A new model for multiscale modeling of the Martian atmosphere, GM3, *J. Geophys. Res.*, *110*, E04001, doi:10.1029/2004JE002354.

Nair, H., M. Allen, A. D. Anbar, Y. L. Yung, and R. T. Clancy (1994), A photochemical model of the Martian atmosphere, *Icarus*, *111*, 124–150.

Ockert-Bell, M. E., J. F. Bell III, J. B. Pollack, C. P. McKay, and F. Forget (1997), Absorption and scattering properties of the Martian dust in the solar wavelengths, *J. Geophys. Res.*, *102*, 9039–9050.

Pollack, J. B., C. B. Leovy, P. W. Greiman, and Y. Mintz (1981), A Martian general circulation experiment with large topography, *J. Atmos. Sci.*, *38*, 3–29.

Rose, K. (1983), On the influence of nonlinear wave-wave interaction in a 3-D primitive equation model for sudden stratospheric warmings, *Beitr. Phys. Atmos.*, *56*, 14–41.

Rybicki, G. B., and D. G. Hummer (1991), An accelerated lambda iteration method for multilevel radiative transfer, 2. Overlapping transitions with full continuum, *Astron. Astrophys.*, *262*, 209–215.

Shapiro, R. (1970), Smoothing, filtering, and boundary effects, *Rev. Geophys.*, *8*, 359–387.

Shepherd, T. G., K. Semeniuk, and J. N. Koshyk (1996), Sponge layer feedbacks in middle-atmosphere models, *J. Geophys. Res.*, *101*, 23,447–23,464.

Smith, M. D., J. C. Pearl, B. J. Conrath, and P. R. Christensen (2001), Thermal Emission Spectrometer results: Mars atmospheric thermal structure and aerosol distribution, *J. Geophys. Res.*, *106*, 23,929–23,945.

Sonnemann, G. R., and M. Grygalashvyly (2003), The zonal wind effect on the photochemistry within the mesosphere/mesopause region, *Adv. Space Res.*, *32*, 719–724.

Takacs, L. L., and R. Balgovind (1983), High latitude filtering in global grid point models, *Mon. Weather Rev.*, *111*, 2005–2015.

Takahashi, Y. O., H. Fujiwara, H. Fukunishi, M. Odaka, Y. Hayashi, and S. Watanabe (2003), Topographically induced north-south asymmetry of the meridional circulation in the Martian atmosphere, *J. Geophys. Res.*, *108*(E3), 5018, doi:10.1029/2001JE001638.

Tomasko, M. G., L. R. Doose, M. Lemmon, P. H. Smith, and E. Wegryn (1999), Properties of dust in the Martian atmosphere from the imager on Mars Pathfinder, *J. Geophys. Res.*, *104*, 8987–9007.

Villanueva, G. L. (2004), The high resolution spectrometer for SOFIA-GREAT: Instrumentation, atmospheric modeling and observations, Ph.D. thesis, Albert-Ludwigs-Universität, Freiburg, Germany.

Wilson, R. J. (1997), A general circulation model of the Martian polar warming, *Geophys. Res. Lett.*, *24*, 123–126.

Wilson, R. J., and K. Hamilton (1996), Comprehensive model simulation of thermal tides in the Martian atmosphere, *J. Atmos. Sci.*, *53*, 1290–1326.

Zhang, D., and R. A. Anthes (1982), A high-resolution model of the planetary boundary layer—Sensitivity tests and comparisons with SESAME-79 data, *J. Appl. Meteorol.*, *21*, 1594–1609.

U. Berger, Leibniz-Institute of Atmospheric Physics, Ostseebad Kühlungsborn, D-18225, Germany. (berger@iap-kborn.de)

A. G. Feofilov and A. A. Kutepov, Institute for Astronomy and Astrophysics, University of Munich, Munich, D-81679, Germany. (artf@usm.uni-muenchen.de; aak@usm.uni-muenchen.de)

P. Hartogh, T. Kuroda, A. S. Medvedev, R. Saito, and G. Villanueva, Max Planck Institute for Solar System Research, Katlenburg-Lindau, D-37191, Germany. (paul@mps.mpg.de; kuroda@mps.mpg.de; medvedev@mps.mpg.de; saito@mps.mpg.de; villanueva@mps.mpg.de)